# High-quality parallel entangling gates in long mixed-species ion chains

Lin Cheng [1,2] Sheng-Chen Liu [1] Gui-Zhong Yao [1,2] Ying-Xiang Wang [1]
Liang-You Peng [1,2,3,*] and Qihuang Gong[1,2,3]

[1]*State Key Laboratory for Mesoscopic Physics and Frontiers Science Center for Nano-optoelectronics,*
*School of Physics, Peking University, 100871 Beijing, China*
[2]*Beijing Academy of Quantum Information Sciences, Beijing 100193, China*
[3]*Collaborative Innovation Center of Extreme Optics, Shanxi University, 030006 Taiyuan, China*

A universal quantum computer is an ultimate pursuit, which should possess the ability to perform entangling gate operations in parallel with high quality in a scalable fashion. However, for a long trapped-ion chain, the simultaneous implementation of two-qubit quantum gates is a challenging task due to the drastic increase of the crosstalk resulting from the collective motional modes. In this paper, by utilizing the structure of the localized motional modes in the long mixed-species ion chain, we propose a highly efficient linear iterative scheme to eliminate the crosstalk within the neighboring pairs. We show that this scheme allows the realization of high-fidelity, low-crosstalk, scalable, parallel two-qubit gates with only a few pulse segments for the long chain. In addition, by considering the practical experimental feasibility, we optimize the laser power and improve the robustness against the random static drifts of the motional frequencies.

## I. INTRODUCTION

In gate-based quantum computing, quantum algorithms can be decomposed into quantum circuits consisting of a series of single-qubit rotations and two-qubit entangling gates. The realization of quantum algorithms (e.g., the Shor's algorithm [1]) requires numerous quantum gates and physical qubits. Parallel entangling gates can provide significant improvement in the execution time of the entire circuits. Additionally, in the fault-tolerant quantum computation, executing parallel two-qubit gates is especially advantageous to quantum error-correction (QEC) codes [2,3], which demand multiple physical qubits to encode a logical qubit and to protect against errors at the physical qubit level.

The ability to perform entangling operations in parallel with low errors in a scalable fashion is a central element of quantum information processing and is an exciting frontier. In recent years, researchers have made significant progress toward building a practical quantum computer with high-quality parallel gates by utilizing various physical platforms such as trapped ions [4,5], superconducting qubits [6], neutral atoms [7,8], and others. The trapped-ion system is one of the most promising platforms for large-scale, fault-tolerant quantum computing due to many beneficial characteristics [9,10], such as the longest coherence time [11], and the high-fidelity single-qubit [12], two-qubit [13–15] or multiqubit entangling gates [4,5,16,17]. Several schemes of parallel quantum gates with a few qubits have been demonstrated [4,5].

However, the scalability and, particularly, the parallel gate operations in a long chain are extremely challenging due to the progressively dense motional modes and complex experimental implementation conditions. The single-mode approach [18] becomes slow for spectrally resolving a certain mode and significant errors will be caused due to unwanted interactions among different modes. An alternative approach was proposed [19,20] in which a high fidelity can be achieved, since the optical forces simultaneously couple to all modes and then the suppression of unwanted interaction can be realized without slowing down the gate. In previous studies, amplitude-modulated (AM) gates [19–22], phase-modulated (PM) gates [16,23–25], frequency-modulated (FM) gates [26–28], and their combinations [29–31] have been developed and demonstrated in a discrete or continuous way. Unfortunately, this multiple-mode approach is a highly nonlinear optimization problem and demands complex experimental implementation conditions [22], which is also difficult for scaling up.

When multiple gates are simultaneously executed, the unwanted interactions (i.e., the crosstalk) among different qubits will degrade the performance of gates and significantly impair the reliability of the whole algorithm. The crosstalk results from the collective motional modes and the corresponding all-to-all interactions, in contrast to the advantage of the full connectivity in the construction of global quantum gates [16]. Additionally, to find a high-fidelity and low-crosstalk gate solution in a long chain is extremely difficult by either the analytic methods or the numerical optimization techniques because of the increase of the nonlinear constraints [4,17].

Therefore, it is a great concern to simultaneously implement two-qubit gates with the least amount of experimental resources in a long chain. Some preliminary theoretical attempts have been recently made for a small number of the same-species ions [5,17]. In Ref. [5], an exact protocol has
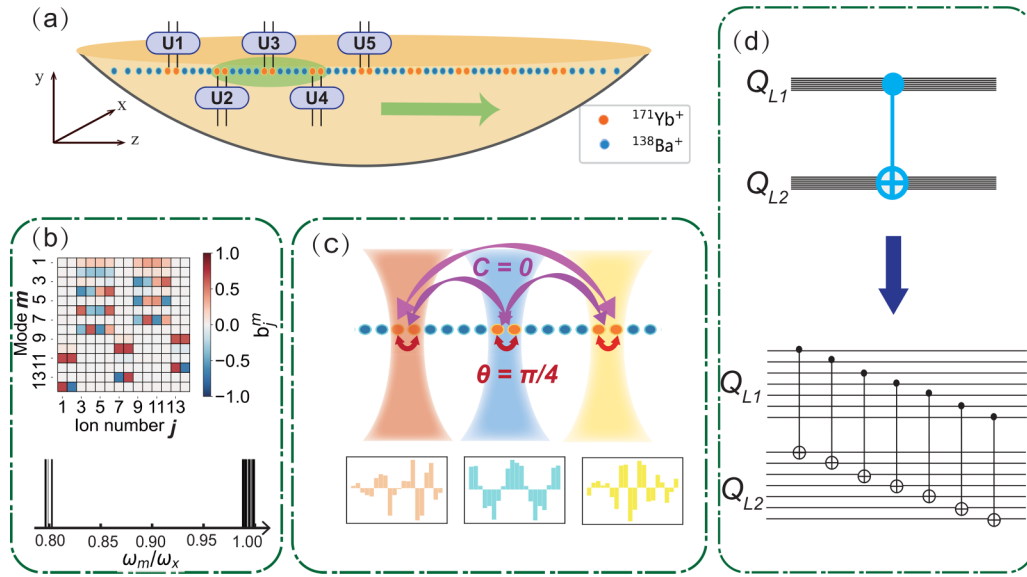
*liangyou.peng@pku.edu.cn

FIG. 1. The implementation of high-fidelity and low-crosstalk parallel two-qubit quantum gates. (a) The periodic $^{171}$Yb$^+$ / $^{138}$Ba$^+$ mixed-species ion chain where $^{171}$Yb$^+$ acts as computational qubits and $^{138}$Ba$^+$ as ancillary qubits. (b) The localized transverse motional modes (top) and the gapped mode frequencies (bottom) of the shadowed subset in the chain. The oscillation amplitude and direction of ions are represented by the color of the squares. (c) The optimized results for the shadowed subset in the chain. The purple and red double-headed arrows, respectively, represent the crosstalk within the three pairs and the degree of entanglement for each pair. The optimal pulses of the three different pairs are plotted in the bottom. (d) One of the possible applications for the logical CNOT gate with the Steane code in QEC.

been devised, which implements simultaneously entangling gates demanding enough pulse segments of the equally segmented AM method. In Ref. [17], the authors used numerical optimization to obtain the solution of high-fidelity, parallel, robust gates only up to 20 ions with amplitude and phase modulation.

In this paper, we utilize the localized motional modes of the mixed-species ion chain [32,33] to improve the scalability and greatly reduce the number of constraints of quantum gates and the pulse complexity. More importantly, we propose a linear iterative scheme to implement high-quality parallel quantum gates which demands only a small amount of pulse segments. Note that our iterative approach is scalable, which is even valid for infinite long uniform ion chains. As shown in Fig. 1(a), we consider a mixed-species ion chain of $^{171}$Yb$^+$ / $^{138}$Ba$^+$ with a periodic-node configuration, which can considerably suppress the overall heating [34]. The computational $^{171}$Yb$^+$ ion pairs are evenly distributed and separated by $P$ ancillary $^{138}$Ba$^+$ ions with several buffer ions at each edge. This ion configuration can be experimentally realized by the ion reordering technique [32].

The mixed-species chain is a powerful platform and yields several advantages suitable for particular tasks [35–37]. In our scheme, the ancillary $^{138}$Ba$^+$ ions have many applications, such as sympathetically cooling the computational ions to effectively suppress the axial motional heating effect [38], performing the independently optimized gates simultaneously on different species ion pairs to realize a maximally dense quantum circuit, keeping memory qubits undisturbed while manipulating other qubits to undergo logic operations [35,36], low addressing errors of qubits with different energy splittings, etc.

Our goal is to perform high-quality two-qubit gates on all pairs of computational ions in parallel by only a few pulse segments, substantially reducing with the pulse complexity. Note that the present ion configuration ensures a successful implementation of parallel entangling gates, thanks to the localized motional modes and the gapped mode frequencies due to the mass difference of two-species ions, as shown in Fig. 1(b) for shadowed ions in Fig. 1(a). The analogous modes can be generated in linear Paul traps with optical tweezer arrays [39].

Here, we propose a linear iterative approach to eliminate the crosstalk within the neighboring pairs in the subset shadowed in Fig. 1(a). This is valid to mitigate the total crosstalk due to the fact that the crosstalk with two simultaneous gates falls off as the inverse cube of the distance between the two pairs in a long chain [30]. As illustrated in Fig. 1(c), the crosstalk between pairs in the subset can be effectively eliminated to 0, with an arbitrary degree of entanglement (e.g., $\frac{\pi}{4}$) specified to every ion pair. For the realization in experiments, we optimize the laser power and assume the same sequence of Rabi frequencies for the two ions in the same pairs, as plotted in the bottom part of Fig. 1(c).

Before presenting the details of our proposal and demonstrating its powerfulness, we want to emphasize that the present parallel entangling gates will have many potential applications. One example is the Steane code [3], which uses seven physical qubits to encode one logical qubit. The logical CNOT gate appears everywhere in quantum algorithms that can be realized transversally, as shown in Fig. 1(d). Compared with serial gates, the parallelism of seven physical CNOT gates can greatly speed up the computation and reduce the error in the QEC circuits.

The rest of this paper is organized as follows: In Sec. II, we will give a brief introduction of the parallel two-qubit entangling gates in a long ion chain. In Sec. III, we will present in detail the localized modes and the corresponding frequencies of the mixed-species finite ion chain and the infinite long uniform ion chain. In Sec. IV, we will propose a linear iterative optimization scheme to achieve the efficient parallel quantum gates with high fidelity and low crosstalk. And in Sec. V, we will discuss the optimized results and compare the crosstalk of different iterative period to show the effectiveness. We also present the results of the uniform ion chain to show that our iterative scheme is scalable and can be generalized to an ion chain of an arbitrary length. Finally, we will summarize our main results and give an outlook in Sec. VI.

## II. THEORETICAL MODEL OF PARALLEL GATES

To realize parallel entangling gates, we adopt the Mølmer-Sørensen gates, which are mediated by the collective motional modes through spin-dependent optical forces [19,21]. The time-evolution operator of the system at gate duration $\tau$ is given by [22]

$$\hat{U}(\tau) = \exp\left\{ \sum_{j,m} \left( \alpha_j^m(\tau)\hat{a}_m^\dagger - \alpha_j^{m*}(\tau)\hat{a}_m \right)\hat{\sigma}_x^j \right.$$
$$\left. + i \sum_{j<j'} \theta_{j,j'}(\tau)\hat{\sigma}_x^j\hat{\sigma}_x^{j'} \right\}, \quad (1)$$

where $\hat{\sigma}_x^j$ is the Pauli spin-flip operator, $\hat{a}_m^\dagger$ and $\hat{a}_m$ are, respectively, the creation and the annihilation operator acting on the $m$th mode, and $\alpha_j^m(\tau)$ is the residual coupling between the internal qubit state of the $j$th ion and the $m$th motional mode,

$$\alpha_j^m(\tau) = -i\eta_j^m \int_0^\tau \Omega_j(t)\sin(\mu t)e^{i\omega_m t}dt, \quad (2)$$

with $\mu$ being the laser detuning and $\Omega_j(t)$ the two-photon Rabi frequency of the $j$th ion. The coupling strength $\theta_{j,j'}(\tau)$ between the $j$th and the $j'$th qubit is given by

$$\theta_{j,j'}(\tau) = 2\sum_m \eta_j^m \eta_{j'}^m \int_0^\tau dt_2 \int_0^{t_2} dt_1 \Omega_j(t_2)\Omega_{j'}(t_1)$$
$$\times \sin(\mu t_1)\sin(\mu t_2)\sin[\omega_m(t_1 - t_2)], \quad (3)$$

where the Lamb-Dicke parameter $\eta_j^m = b_j^m \Delta k_j \sqrt{\frac{\hbar}{2m_{\text{ion}}^j \omega_m}}$ couples the $j$th ion with the $m$th transverse mode where $b_j^m$ is the mode eigenvector for mode frequency $\omega_m$, $m_{\text{ion}}^j$ is the mass of the $j$th ion, and $\Delta k_j$ is the difference of two wave vectors. For the qubit transitions of $^{171}$Yb$^+$ ($^{138}$Ba$^+$), the lasers have a wavelength around $\lambda = 355$ nm (532 nm), which can keep one species of ions undisturbed while manipulating the other. In Eq. (3), the summation over $m$ is limited to the transverse $x$ modes, which is preferable for entangling operations due to less susceptibility to the heating [21].

To perform ideal-fidelity and no-crosstalk parallel entangling operations involving $N_1$ independent pairs of qubits in a chain of $N$ ions ($N \geqslant 2N_1$), we require

$$\alpha_j^m(\tau) = 0, \quad \forall j, m, \quad (4)$$

$$\theta_{j,j'}(\tau) = \begin{cases} \pm\pi/4, & [j, j'] \in J \\ 0, & [j, j'] \in J', \end{cases} \quad (5)$$

where $J$ is the set of $N_1$ pairs of neighboring ions on which parallel gates are to be performed and the set $J'$ contains all ordered pairs that are not included in $J$, whose interactions represent the crosstalk.

Hence, there are a total number of $4N_1 \times N + 2N_1(2N_1 - 1)/2$ constraints to be satisfied. It is almost impossible to find analytical solutions to this nonconvex quadratically constrained problem, which is NP hard in general [4,16]. One may attempt to find optimal solutions by numerical optimization techniques for a small number of ions [4,16,17]. However, these methods soon become inefficient and impractical with the nonlinear increase of the constraints for a long ion chain, due to the demanding computation resources, the loss of fidelity, and the increase of crosstalk, and the pulse complexity.

To overcome these difficulties, we propose a linear iterative method to design high-quality parallel entangling gates for a long mixed-species ion chain. For this, we adopt the discrete AM method [19,22] and define a real column vector $\boldsymbol{\Omega} = (\Omega_1, \Omega_2, ..., \Omega_{N_{\text{seg}}})^T$, where $\tau$ is equally divided into $N_{\text{seg}}$ segments and the amplitude in each segment is independently modulated to fulfill the above mentioned constraints. The matrix form of the constraints in Eqs. (4) and (5) can be given as follows:

$$\mathbf{M}^j\boldsymbol{\Omega}^j = \mathbf{0}, \quad j = 1, ..., 2N_1, \quad (6)$$

$$\theta_{j,j'}(\tau) = (\boldsymbol{\Omega}^j)^T \mathbf{D}^{[j,j']}\boldsymbol{\Omega}^{j'}, \quad (7)$$

where $\mathbf{M}^j$ is the $2N \times N_{\text{seg}}$ coefficient matrix, $\mathbf{D}^{[j,j']}$ is the $N_{\text{seg}} \times N_{\text{seg}}$ matrix, and $\boldsymbol{\Omega}^j$ is the amplitude vector of length $N_{\text{seg}}$ of the $j$th qubit. The explicit expressions of $\mathbf{M}^j$ and $\mathbf{D}^{[j,j']}$ are given in Appendix A. As can be seen, the spin-motion decoupling constraints are linear with respect to the control laser parameters, while the coupling strength constraints are quadratic.

We use three types of gate imperfections to measure the gate performance [39], i.e., the average infidelity per gate $\delta F$ which is related to the residual spin-motion coupling, the over- or underaccumulated phase errors per gate $\delta\chi$, and the average crosstalk per gate $C$ for pairs contained in $J'$,

$$\delta F = \frac{4}{5N_1} \sum_{[j,j']\in J} \sum_m \left( |\alpha_j^m|^2 + |\alpha_{j'}^m|^2 \right)[2\bar{n}_m + 1], \quad (8)$$

$$\delta\chi = \frac{2}{N_1} \sum_{[j,j']\in J} \left| |\theta_{j,j'}| - \frac{\pi}{4} \right|, \quad (9)$$

$$C = \frac{2}{N_1} \sum_{[j,j']\in J'} |\theta_{j,j'}|, \quad (10)$$

where we take the averaged phonon number of the $m$th mode $\bar{n}_m \approx 0.5$.

## III. MOTIONAL MODES OF THE MIXED-SPECIES ION CHAIN

A mixed-species chain of ions is crucial for scaling trapped-ion quantum computers and communication networks. In this section, we present the motional modes $b_j^m$ and mode frequencies $\omega_m$ for the mixed-species ion chain of $^{171}$Yb$^+$ / $^{138}$Ba$^+$, which play an important role in the design of parallel quantum gates. In this paper, we consider a
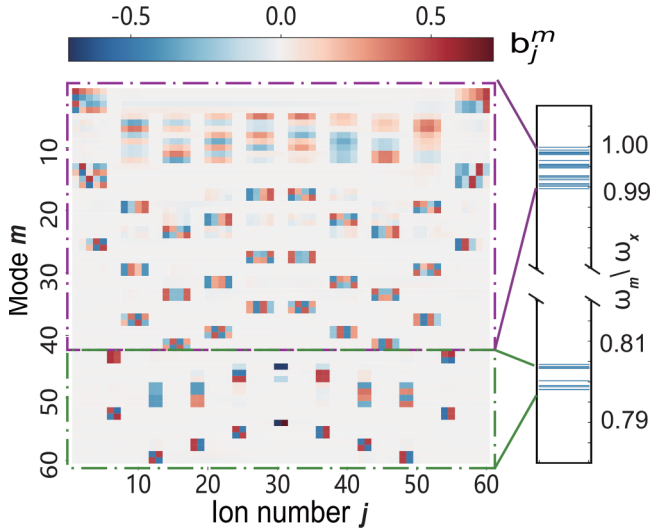
FIG. 2. The transverse motional modes $b_j^m$ ($j, m = 1, \ldots, 60$) for a chain of 60 ions with $P = 4$. The mode frequency spectrum $\omega_m/\omega_x$ is shown on the right side, respectively, corresponding to the higher (for the purple box) and lower frequencies (for the green box).

chain of 60 ions with five buffer ions at each edge trapped in a hybrid potential with $\gamma_4 = 0.461$ and choose the ion period distance $P = 4$ to implement nine entangling pairs in total. To achieve an average spacing of $d = 10 \, \mu m$, we choose the trapping frequency $\omega_x = \omega_y = 2\pi \times 2.28$ MHz and $\omega_z = 2\pi \times 8.47$ kHz. The transverse motional modes and the corresponding frequencies can be precisely calculated; see Appendix B for details.

As shown in Fig. 2, the transverse motional modes and the corresponding frequencies drastically differ from those for the same-species chain [32]. One of the important features is that the motion of $^{171}$Yb$^+$ is almost completely decoupled from that of $^{138}$Ba$^+$ so the motional modes of the two-species ions are localized and independent. Thus, the crosstalk between these two species of ions is naturally suppressed. Additionally, for symmetric computational pairs with respect to the center of the trap, their localized modes are hybridized due to the long-range residual Coulomb interaction and the reflection symmetry. In addition, the motion of each asymmetric ion pair is mutually independent, which only consists of several localized center-of-mass and stretch modes. Finally, the mode frequencies of the mixed-species chain are gapped and split up into several subsets. Note that the frequencies are degenerate for two symmetric pairs which dominate the corresponding motional modes. The features of motional modes for the infinite long uniform ion chain are similar to the finite ion chain, whose details can be found in Appendix B.

These different features are not only related to the mass difference, but also to the relative contributions of the ponderomotive and the static potential of the confinement to the ions [32]. Our linear iterative method to implement parallel gates is performed on a long periodic chain of $^{171}$Yb$^+$/$^{138}$Ba$^+$. However, our scheme is readily generalized to other mixed species with different masses, such as $^9$Be$^+$/$^{25}$Mg$^+$, $^{40}$Ca$^+$/$^{88}$Sr$^+$, $^9$Be$^+$/$^{40}$Ca$^+$, etc. Therefore, the difference between the two species can be a powerful tool

and makes it possible for a multispecies trapped ion system to deal with some tasks that are difficult for a single species trapped ion system. We list some important applications of the mixed-species ion chain in our scheme in Appendix C.

## IV. THE LINEAR ITERATIVE APPROACH

To suppress the crosstalk within the same-species ion pairs and improve the gate fidelity, we propose a linear iterative approach to design scalable high-quality parallel gates. Our scheme can be divided into two steps. The first step is the construction of the approximated null space (ANS) which guarantees the high gate fidelity. Second, we eliminate the crosstalk within the neighboring ion pairs by constructing a subspace of ANS orthogonal to the interactions between the considered pair and the preceding ion pairs whose pulse shapes are already determined.

### A. The high fidelity

First, for each entangled ion pair $[j_n, j_n'] \in J$ ($n = 1, \ldots, N_1$), we construct an ANS $\boldsymbol{\Omega}_{\mathrm{ans}}^{[j_n, j_n']}$ with dimension $N_{j_n}$ as the solution space at the cost of a negligible amount of fidelity. We relax the spin-motion decoupling constraints Eq. (6) into $\mathbf{M}^j \boldsymbol{\Omega}^j \approx \mathbf{0}$, which means that we do not require an exact solution of ideal fidelity but rather just ensure that the infidelity induced by the imperfect pulse shape is much smaller than the other error sources [40]. There are several reasons for constructing ANS at a cost of a negligible amount of fidelity. First, the fidelity of two-qubit gates in current experiments is around 99.9% due to the laser intensity fluctuations, the motional-mode heating, and other noises [26,31,41]. Meanwhile, we notice that some eigenvalues of the spin-motion matrix are particularly small in the magnitude and the corresponding eigenvectors (with a suitable normalization) are experimentally favorable solutions, such as an obvious decrease of the laser power or the smoothing of the pulse shape.

In our scheme, we assume the pulse shapes to be the same for two neighboring ions in the same computational ion pair, which can be more easily achieved in experiments, i.e., $\boldsymbol{\Omega}^{j_n} = \boldsymbol{\Omega}^{j_n'} = \boldsymbol{\Omega}^{[j_n, j_n']}$. Therefore, the calculation of ANS is based on the spin-motion decoupling matrix of two ions in the same pair in $J$. The $\boldsymbol{\Omega}_{\mathrm{ans}}^{[j_n, j_n']}$ can be obtained by including the eigenvectors of matrix $\mathbf{M}^{[j_n, j_n']}$,

$$\mathbf{M}^{[j_n, j_n']} = (\mathbf{M}^{j_n})^{\dagger}(\mathbf{M}^{j_n}) + (\mathbf{M}^{j_n'})^{\dagger}(\mathbf{M}^{j_n'}), \qquad (11)$$

where $[j_n, j_n'] \in J$ is the ion number in the same computational ion pairs.

For ion pair $[j_n, j_n']$, through the eigenvalue decomposition of $\mathbf{M}^{[j_n, j_n']}$, we obtain its eigenvalues $\lambda_1, \lambda_2, \ldots, \lambda_{N_{\mathrm{seg}}}$, ordered according to their absolute values, together with their corresponding eigenvectors $\boldsymbol{\Omega}_1, \boldsymbol{\Omega}_2, \ldots, \boldsymbol{\Omega}_{N_{\mathrm{seg}}}$. The eigenvector $\boldsymbol{\Omega}_i$ which is scaled by the corresponding degree of entanglement, i.e., $\boldsymbol{\Omega}_i \to \sqrt{\frac{\pi}{4|C|}} \boldsymbol{\Omega}_i$ will then yield an infidelity with $\boldsymbol{\Omega}_i^T \mathbf{D}^{[j_n, j_n']} \boldsymbol{\Omega}_i = C$ ($i = 1, \ldots, N_{\mathrm{seg}}$). The scaled eigenvectors whose infidelity is below the infidelity threshold $\delta F_t$ form an orthogonal basis of the ANS $\boldsymbol{\Omega}_{\mathrm{ans}}^{[j_n, j_n']}$. In this paper, we set $\delta F_t = 10^{-4}$, which is acceptable in current experiments.

We define the ANS $\mathbf{\Omega}_{\mathrm{ans}}^{[j_n,j_n']}$ as an $N_{\mathrm{seg}} \times N_{j_n}$ matrix, whose columns $(\mathbf{\Omega}_{\mathrm{ans}}^{[j_n,j_n']})_{n_j}$ form an orthogonal basis of the space where $n_j = 1, ..., N_{j_n}$ and $N_{j_n}$ is the number of the scaled eigenvectors whose infidelity is below the $\delta F_t$. Using the $N_{j_n}$ degrees of freedom, we can reduce the total crosstalk within the ion pairs and obtain experimentally favorable solutions, such as the decreasing of the laser power or the smoothing of the pulse shape. Note that the ANS of every pair is different due to the localized modes.

Before discussing the second step, we would like to point out one of the advantages of the current scheme. For a mixed-species long chain, the ANS of every pair can be easily constructed using much fewer pulse segments $N_{\mathrm{seg}}$, compared with that for the same-species chain. We can achieve the two-qubit gate for every pair at a low infidelity around $10^{-5}$ with $N_{\mathrm{seg}}$ slightly greater than 4 and achieve gates with an ideal fidelity 1 with $N_{\mathrm{seg}}$ far less than $2N$ that is required for the same-species ion chain [5] due to the degeneracy and the localization of the motion modes. The dominant contribution to the infidelity is caused by the unclosed phase-space trajectories of modes for the motion of other asymmetric ion pairs. The motional modes of the ancillary ions scarcely have any effects on the fidelity since the gapped higher mode frequencies are far detuned with $\mu$.

### B. The low crosstalk

Second, on the basis of the first step, we choose a crosstalk iterative period which includes $G$ neighboring pairs and divide the $N_1$ pairs into several subsets, i.e., $\{l+1, l+2, ..., l+G\}$, where $l = 0, 1, ..., N_1 - G$. We apply an iterative method to eliminate the crosstalk within the pairs in the same subset. We construct a subspace of ANS for the considered pair, which is orthogonal to the interactions between this pair and the preceding ion pairs whose pulse shape are already determined. The pulse shape of this pair is then determined by the power-optimal method with the approximated null subspace $\mathbf{\Omega}_{\mathrm{anss}}$.

The approximated null subspace $\mathbf{\Omega}_{\mathrm{anss}}^{[j_n,j_n']}$ is spanned by $\sum_{n_j}(\mathbf{\Lambda}_\nu^{[j_n,j_n']})_{n_j}(\mathbf{\Omega}_{\mathrm{ans}}^{[j_n,j_n']})_{n_j}$, where $n_j = 1, ..., N_{j_n}$ and $\nu = 1, ..., V_{j_n}$, where $V_{j_n}$ is the dimension of $\mathbf{\Omega}_{\mathrm{anss}}^{[j_n,j_n']}$. For instance, if we would like to eliminate the crosstalk between two pairs $[j_m, j_m']$, $[j_n, j_n']$, where the pulse shape $\mathbf{\Omega}^{[j_m,j_m']}$ of $[j_m, j_m']$ is determined, it requires

$$\theta[j_m, j_n] = \theta[j_m, j_n'] = \theta[j_m', j_n] = \theta[j_m', j_n'] = 0, \quad (12)$$

where $\theta[j_m, j_n] = \mathbf{K}^{[j_m,j_n]}\mathbf{\Lambda}^{[j_n,j_n']}$, $\mathbf{K}^{[j_m,j_n]} = (\mathbf{\Omega}^{[j_m,j_m']})^T$ $\mathbf{D}^{[j_m,j_n]}\mathbf{\Omega}_{\mathrm{ans}}^{[j_n,j_n']}$ is an $N_{j_n}$-dimension row vector.

Therefore, for the $g$th pair in the $l$th subset for which the pulse shapes of the preceding $(g-1)$ ion pairs are already determined, there exists $4 \times (g-1)$ crosstalk constraints. To eliminate the crosstalk, one requires

$$\mathbf{K}\mathbf{\Lambda}^{[j_{g,l},j_{g,l}']} = \mathbf{0}, \quad (13)$$

where $\mathbf{K}$ is $(4 \times (L-1)) \times N_{j_{g,l}}$ matrix. We label the ion pair of the $g$th pair in the $l$th subset as $(g, l)$ for $g = 1, ..., G$ and $l = 0, 1, ..., N_1 - G$.

The important issue is the degree of freedom. We have $N_{j_{g,l}}$ variables and $4 \times (g-1)$ constraints according to Eq. (13), so

$N_{j_{g,l}}$ for the $g$th pair in the $l$th subset has a lower limit, $N_{j_{g,l}} > 4 \times (g-1)$. The dimension of $\mathbf{\Lambda}^{[j_{g,l},j_{g,l}']}$ is $V_{j_{g,l}} = N_{j_{g,l}} - (4 \times (g-1))$. When $g$ reaches the maximum value $G$ in the $l$th subset, the segments of pulse need to be enough to guarantee the $N_{j_{G,l}} > (4 \times (G-1))$. Please note that Eq. (13) can be readily solved by Gaussian elimination, the lower upper (LU) decomposition, etc. We then define the approximated null subspace $\mathbf{\Omega}_{\mathrm{anss}}^{[j_{G,l},j_{G,l}']}$ as an $N_{\mathrm{seg}} \times V_{j_{G,l}}$ matrix, whose columns $(\mathbf{\Omega}_{\mathrm{anss}}^{[j_{G,l},j_{G,l}']})_\nu = \sum_{n_j}(\mathbf{\Lambda}_\nu^{[j_{G,l},j_{G,l}']})_{n_j}(\mathbf{\Omega}_{\mathrm{ans}}^{[j_{G,l},j_{G,l}']})_{n_j}$ form an orthogonal basis of the space for $\nu = 1, ..., V_{j_{G,l}}$.

Then we can apply the power-optimal method to obtain the optimal linear combination of $\mathbf{\Omega}_{\mathrm{anss}}$ for the currently considered pair. The details of the power-optimal method [40] is elaborated in Appendix D. The optimal solution $\mathbf{\Omega}^{[j_{G,l},j_{G,l}']} = \mathbf{\Omega}^{j_{G,l}} = \mathbf{\Omega}^{j_{G,l}'}$ can be written down explicitly with coefficients $\Gamma_\nu$:

$$\mathbf{\Omega}^{[j_{G,l},j_{G,l}']} = \sum_{\nu=1}^{V_{j_{G,l}}} \Gamma_\nu (\mathbf{\Omega}_{\mathrm{anss}}^{[j_{G,l},j_{G,l}']})_\nu. \quad (14)$$

The pulse shapes of the $(G-1)$ ion pairs have already been determined in the same subset except for the first subset. More details of the first subset are necessary to be explained. For the first pair, the pulse shape is directly determined by the power-optimal method with the ANS without considering the crosstalk constraints. For the subsequent pairs, we construct the subspace of ANS to eliminate the crosstalk between it and the previous pairs. Once the pulse shapes for the first subset are determined, we can continue to the next subset which is more simple due to the previous determined $G-1$ pairs.

Except to the power optimization, we can also reduce the pulse gradient which is the amplitude change between any two adjacent segments of the pulse in the AM method [40]. As the laser amplitudes are equally segmented in discrete time intervals and abrupt changes in laser amplitudes are hard to be physically realized, especially when one performs the fast gates. Therefore, the optimization of the pulse gradient is important in experiments.

It should be noted that our iterative scheme is highly scalable, which is even valid for an infinite long uniform long chain. The iterative approach for the infinite long uniform ion chain can still be divided into two steps, as has been done for the finite ion chain. First, for each entangled computational ion pair, we construct an ANS $\mathbf{\Omega}_{\mathrm{ans}}$ as the solution space in which we draw pulse shapes yielding an infidelity below a certain threshold value $\delta F_t$. Because of the discrete translational invariance under the transformation of the mixed-species ion chain, the ANS of every pair is the same, which can simplify the calculation. Second, for the iterative approach of the finite ion chain, we determine the pulse shape of every subset from the left end of the chain to the right on the basis of the preceding determined pairs of the last subset. However, the periodicity of the infinite long uniform chain is an advantage. Therefore, we can calculate the pulse shape of one of the subsets and the resulting Rabi sequences are applied periodically in space. We can also construct a subspace of ANS which eliminates the crosstalk within the neighboring pairs in the subsets.
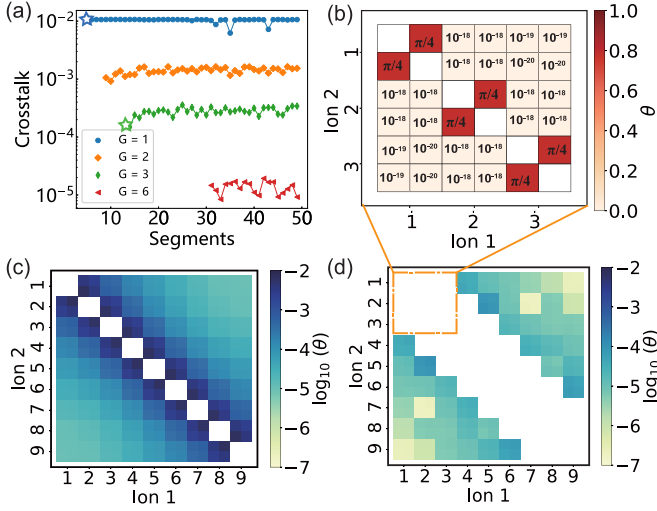
FIG. 3. (a) The crosstalk $C$ as a function of the pulse segments $N_{\rm seg}$ for different iterative periods $G$. (b) The coupling strength $\theta$ within ions in the first subset, as indicated in (d). (c) The coupling strength $\theta$ within ions for each computational pairs for the case $N_{\rm seg} = 5$ and $G = 1$, highlighted by blue star in (a). Both axes represent the numbering of the nine computational pairs. (d) The coupling strength $\theta$ for $N_{\rm seg} = 14$ and $G = 3$, indicated by the green star in (a).

## V. NUMERICAL RESULTS

In this section, we demonstrate the effectiveness of our scheme by an example with the detuning $\mu = 0.802\,\omega_x$ and the gate duration $\tau = 100\,\mu$s. As seen in Fig. 3(a), the total crosstalk decreases quickly as one increases the iterative period $G$, which confirms that the crosstalk with neighboring pairs is fully eliminated, as can be observed in Fig. 3(b). As mentioned previously, since the lower limit of the dimension of ANS increases with $G$, there exist different minimal numbers of pulse segments for every $G$, as seen in Fig. 3(a). In addition, once the required number of $N_{\rm seg}$ is satisfied, a further increase of $N_{\rm seg}$ has little effect on the average crosstalk per gate.

To show how our iterative approach reduces the total crosstalk, we can compare the results for $G = 1$ and 3, for which we obtain an infidelity of $2.4 \times 10^{-6}$ and $1.2 \times 10^{-6}$, respectively, well below the threshold $\delta F_t$. The specified entanglement of every two-qubit gate is exactly achieved. In addition, the crosstalk for $G = 3$ is $C_{G=3} = 1.5 \times 10^{-4}$, much smaller than $C_{G=1} = 1.1 \times 10^{-2}$.

The advantages can also be seen by comparing the coupling strength $\theta$ within ions for each of computational pairs. For the case of $G = 1$ without the crosstalk elimination, as shown in Fig. 3(c), the crosstalk within the neighboring pairs of ions is the dominant source. On the contrary, for $G = 3$, the crosstalk between pairs in the subset has been fully eliminated, as shown in Fig. 3(d) and enlarged in Fig. 3(b). The remaining small crosstalk comes from the interaction between ion pairs whose distance is larger than the maximum distance in the iterative period.

As $G$ increases, more crosstalk constraints are added and then the vectors of the solution space that can lower the laser power will be reduced, which will lead to an increase of the
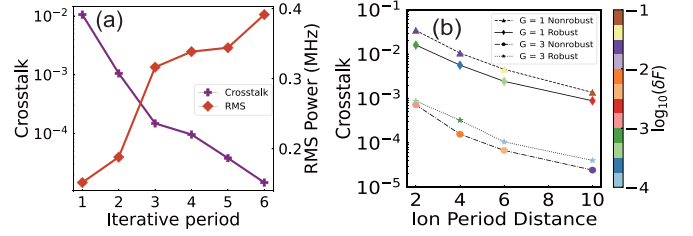


FIG. 4. (a) The crosstalk $C$ as a function of $G$ and the correspondingly required RMS power for the minimal pulse segments $N_{\rm seg} = 5, 9, 14, 20, 22, 31$. (b) The crosstalk $C$ for $G = 1$ and 3 as the function of $P$ for the robust and the nonrobust pulse, respectively. The color of markers represents the average infidelity when the motional-mode frequencies randomly drift with different signs of $\delta\omega_c$. Note that we change the total number of ions to keep the number of two-qubit gates at nine. For each $P$, the number of pulse segments is the same, i.e., for $G = 1, 3$, we take $N_{\rm seg} = 5, 14$ for the nonrobust pulse and $N_{\rm seg} = 7, 20$ for the robust pulse, respectively.

laser amplitude. However, in our scheme, we determine each pulse shape using the power-optimal method. As observed in Fig. 4(a), the increase of the iterative method can significantly reduce the average crosstalk, but only at the cost of a reasonable increase of the laser power. Additionally, the crosstalk can also be suppressed by increasing the period distance $P$, as shown in Fig. 4(b).

In addition, it is also a critical issue to construct gates being stabilized against control parameter fluctuations [31]. Our approach is scalable and admits the linear construction of the robust constraints, which is related to the spin-motion decoupling at the cost of additional degrees of freedom. Here, we show the infidelity for the robust and nonrobust gates against the random static drifts of the mode frequencies with uncertainty $\delta\omega_c = 2\pi \times 2000$ Hz. As seen from the color of the markers in Fig. 4(b), we find that the robust pulse significantly improves the fidelity and can tolerate errors dramatically more than the nonrobust case. The infidelity of the robust pulse for $G = 1$ and $P = 4$ is $2.67 \times 10^{-4}$ while the infidelity of nonrobust pulse is $2.98 \times 10^{-2}$. The details of the random static drifts of frequencies and other linear robustness constraints can be found in Appendix E.

To show the scalability of our approach, we present the crosstalk within each pair of computational ions in an infinite long uniform ion chain of the $G = 1$ with the corresponding minimal pulse segments $N_{\rm seg} = 10$ and $G = 3$ with $N_{\rm seg} = 19$ in Figs. 5(a) and 5(b). For convenience, the squares represent the crosstalk with two pairs, $\theta_{\rm pair}$. In both cases, we obtain an average infidelity of $\delta F_{G=1} = 4.29 \times 10^{-6}$ and $\delta F_{G=3} = 5.54 \times 10^{-6}$, respectively, where the infidelity of each ion pair is below $\delta F_t$, which guarantees the average infidelity $\delta F < \delta F_t$. The over- and underaccumulated phase errors are $\delta\chi_{G=1} = \delta\chi_{G=3} = 0$, which means that every two-qubit gate achieve the specified entanglement in our approach. The crosstalk per gate is $C_{G=1} = 3.20 \times 10^{-2}$ and $C_{G=3} = 1.40 \times 10^{-3}$, respectively. As shown in Fig. 5(a) without the crosstalk elimination ($G = 1$), the squares near the diagonal are very dark, which means that the crosstalk within the neighboring pairs of ions is the dominant source of the total crosstalk. This is why we chose our optimization scheme to eliminate
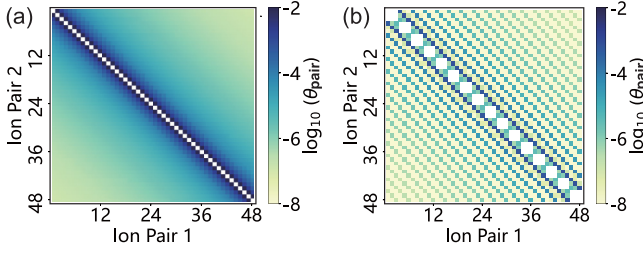
FIG. 5. (a) The coupling strength $\theta_{\text{pair}}$ within computational ion pairs in one of the subsets with $N_{\text{seg}} = 10$, the detuning $\mu = 2\omega_2 - \omega_1$, and the gate duration $\tau = 2\pi/(\omega_1 - \omega_2)$ for $G = 1$. The label represents the number of 48 ion pairs. (b) The coupling strength $\theta_{\text{pair}}$ within computational ion pairs in one of the subsets with $N_{\text{seg}} = 19$, the detuning $\mu = 2\omega_2 - \omega_1$, and the gate duration $\tau = 2\pi/(\omega_1 - \omega_2)$ for $G = 3$.

the crosstalk within neighboring pairs. For the period $G = 3$, the crosstalk between each pair of ions in the subsets is fully eliminated. Additionally, the crosstalk with different pairs in Fig. 5(b) reflects the periodicity of the infinite uniform long ion chain.

## VI. CONCLUSIONS

There are several advantages in the current scheme. In terms of the solution algorithm, our linear iterative scheme can obtain the optimal solution efficiently and have a good stability compared with numerical optimization techniques. Compared with the linear protocol adopted in Ref. [5], we propose an effective iterative scheme to eliminate the crosstalk within the neighboring pairs. Our scheme considers the construction of an approximated null subspace and the robustness constraints. The pulse complexity is substantially decreased. The pulse shape is preferable in experiments which demand a few pulse segments. More importantly, our iterative approach is scalable, which is even valid on infinite long uniform chains.

Nevertheless, there do remain some experimental challenges, such as the ion reordering of mixed-species ions, the ability to reconfigure and interlace the ion chain and arrange qubits into desired pairs, the low efficiency of the sympathetic cooling of transverse modes [32], etc. Compared to the same-species ion chain, the mixed-species ion chain needs a more exquisite control of ion positions and complex electrode design, which presents substantial platform-specific scientific and engineering challenges. The gate fidelity can be limited to extra technical complications, the photon scattering, and the imperfect stray field compensation, etc. However, these experimental challenges would be attempted with the fast advances of relevant technologies [35–37].

In conclusion, we utilize the localized motional modes and the gapped mode frequencies of the mixed-species ion chain to greatly simplify the constraints of gate and lower

the crosstalk. More importantly, we have proposed a highly efficient iterative scheme to eliminate the crosstalk within the neighboring pairs of $^{171}\text{Yb}^+$ and demonstrated its implementation for high-fidelity, low-crosstalk, scalable, and robust parallel two-qubit quantum gates in a long mixed-species chain. In the future, a combination of the present parallel gates with trapping and rearrangement of individual ions in a mixed-species chain may serve as an efficient scheme for error-corrected and fault-tolerant operations to eventually enable a large-scale trapped-ion quantum processor.

## APPENDIX A: MATRIX EXPRESSIONS

In this Appendix, we give the explicit expressions for the constraints.

The spin-motion decoupling constraints Eq. (4) of the $j$th qubit can be written in matrix form as follows:

$$\mathbf{M}^j \mathbf{\Omega}^j = \mathbf{0}. \tag{A1}$$

The elements of matrix $\mathbf{M}^j$ are given by

$$M^j(m, n) = \eta_j^m \int_{t_{n-1}}^{t_n} \sin(\mu t)\sin(\omega_m t)dt$$

$$M^j(m + N, n) = \eta_j^m \int_{t_{n-1}}^{t_n} \sin(\mu t)\cos(\omega_m t)dt, \tag{A2}$$

where $\mathbf{M}^j$ is the $2N \times N_{\text{seg}}$ coefficient matrix, $j$ is the label of the ion, and $t_n = n\tau/N_{\text{seg}}$. $M^j(m, n)$ and $M^j(m + N, n)$ are, respectively, the real and imaginary parts of the residual coupling of the $m$th motional mode.

The coupling strength constraints Eq. (5) between ion pair $[j, j']$ can be written in matrix form:

$$(\mathbf{\Omega}^j)^T \mathbf{S}^{[j,j']} \mathbf{\Omega}^{j'} = \theta_{j,j'}(\tau) = \begin{cases} \theta_{\text{ideal}}, & [j, j'] \in J \\ 0, & [j, j'] \in J', \end{cases} \tag{A3}$$

where $\mathbf{S}^{[j,j']}$ is the $N_{\text{seg}} \times N_{\text{seg}}$ matrix. Since $\theta_{j,j'}(\tau)$ is a scalar, we can further construct a symmetric matrix $\mathbf{D}^{[j,j']} = (\mathbf{S}^{[j,j']} + (\mathbf{S}^{[j,j']})^T)/2$ such that $\theta_{j,j'}(\tau) = (\mathbf{\Omega}^j)^T \mathbf{S}^{[j,j']} \mathbf{\Omega}^{j'} = (\mathbf{\Omega}^j)^T \mathbf{D}^{[j,j']} \mathbf{\Omega}^{j'}$. In this paper, we consider maximally entangling gates with $\theta_{\text{ideal}} = \pm\pi/4$ as a benchmark case, which is important in quantum circuits. However, different and independent values of $\theta_{\text{ideal}}$ can be simply achieved by scaling the Rabi frequencies.

The entanglement matrix $\mathbf{S}^{[j,j']}$ is a real $N_{\text{seg}} \times N_{\text{seg}}$ matrix whose $(p, q)$ element is given by

$$\mathbf{S}^{[j,j']}(p, q) = \begin{cases} 2\sum_m \eta_j^m \eta_{j'}^m \int_{t_{p-1}}^{t_p} dt_1 \int_{t_{q-1}}^{t_q} dt_2 \sin(\mu t_1)\sin(\mu t_2)\sin[\omega_m(t_1 - t_2)], & (p > q) \\ 2\sum_m \eta_j^m \eta_{j'}^m \int_{t_{p-1}}^{t_p} dt_1 \int_{t_{p-1}}^{t_1} dt_2 \sin(\mu t_1)\sin(\mu t_2)\sin[\omega_m(t_1 - t_2)], & (p = q) \\ 0, & (p < q). \end{cases} \tag{A4}$$

## APPENDIX B: MOTIONAL MODES AND FREQUENCIES

### 1. The finite ion chain

In a typical linear Paul trap, the ion confinement is realized by using a combination of direct current and radiofrequency fields with the angular frequency $\Omega_T$. In the pseudopotential approximation, we introduce $\epsilon = \omega_p/\omega_z$ and $\omega_x = \omega_y = \sqrt{\omega_p^2 - \frac{1}{2}\omega_z^2}$. When the potential traps two different species of ions with mass $m_{Ba}$, $m_{Yb}$, the relation of trap frequencies can be expressed,

$$\omega_z^{Yb} = \sqrt{\frac{1}{\mu_m}}\omega_z^{Ba}, \tag{B1}$$

$$\omega_{(x,y)}^{Yb} = \sqrt{\frac{1}{\mu_m}}\sqrt{\frac{\frac{1}{\mu_m}\epsilon^2 - \frac{1}{2}}{\epsilon^2 - \frac{1}{2}}}\omega_{(x,y)}^{Ba}, \tag{B2}$$

where the mass ratio $\mu_m = m_{Yb}/m_{Ba}$. It should be noted that the axial trap frequencies $\omega_z$ simply scale with the square root of the mass ratio and the radial trap frequencies $\omega_{x,y}$ additionally depend on $\epsilon$. The transverse potential depends on the ion's mass and then different species ions feel different trap potentials.

For ions in a linear Paul trap along the axial direction, a suitable hybrid potential consisting of a quadratic and quartic potential with a dimensionless ratio $\gamma_4 = \alpha_4 l_0^2/\alpha_2$ can be applied in the axial direction to achieve a uniform configuration,

$$U = \sum_{i=1}^{N}\left(-\frac{1}{2}\alpha_2 z_i^2 + \frac{1}{4}\alpha_4 z_i^4\right) + \sum_{i<j}\left(\frac{q^2}{4\pi\varepsilon_0|z_i - z_j|}\right), \tag{B3}$$

where $q$ is the charge of an ion, $z_i$ is the axial position of the $i$th ion, $N$ is the number of ions, $\varepsilon_0$ is the permittivity in

the free space, and $\alpha_2$, $\alpha_4$ are the coefficients of the quadratic and quartic term ($\alpha_2$, $\alpha_4 > 0$). For convenience, we rescale the positions $z_i$ using a length scale $l_0^3 = q^2/4\pi\varepsilon_0\alpha_2$ and then define $u_i = z_i/l_0$.

In our scheme, we consider a chain of 60 ions, five of which on each end of the chain are used as buffer ions. We adjust $\gamma_4$ to minimize the relative standard deviation (RSD) for the spacing of the 50 ions. $\gamma_4 = 0.461$ is found to give a minimal RSD of only 2.3%. We can get the equilibrium position $u_i$ of the ions by minimize the axial potential energy. The solution is independent of the mass, as the potential of the electrodes interacts only with the ionic charges.

Specifically, the motional modes and their corresponding mode frequencies can be obtained through the diagonalization of the symmetric Hessian matrix of the total potential energy in a Taylor expansion of the potential around the equilibrium positions. The dynamics of the system is described by the Lagrangian

$$L = \frac{m_{Yb}}{2}\sum_{i=1}^{2N_1}\dot{q}_i^2 + \frac{m_{Ba}}{2}\sum_{i=1}^{N_2}\dot{q}_i^2 - \frac{1}{2}\sum_{i,j=1}^{N}A_{ij}q_iq_j, \tag{B4}$$

where $q_i$ is the displacement of the $i$th ion from the equilibrium position, $2 \times N_1$ is the number of $^{171}Yb^+$, and $N_2 = N - 2 \times N_1$ is the number of $^{138}Ba^+$ in our calculations. $A_{ij} = \frac{\partial^2 V}{\partial q_i \partial q_j}$ is the symmetric Hessian matrix of the potential energy $V$. At this point, it is convenient to switch to mass-weighted coordinates, $Q_{m_{Ba}} = \sqrt{m_{Ba}}q_{m_{Ba}}$, $Q_{m_{Yb}} = \sqrt{m_{Yb}}q_{m_{Yb}}$, which allows the kinetic energy to be written in a form that is independent of mass. The Lagrangian can then be expressed as

$$L = \frac{1}{2}\sum_{i=1}^{N}\dot{Q}_i^2 - \frac{1}{2}\sum_{i,j=1}^{N}A'_{ij}Q_iQ_j, \tag{B5}$$

where $A'_{ij} = \frac{A_{ij}}{\sqrt{m_{ion}^i m_{ion}^j}}$, whose elements are given by

$$A'_{ij} = \left(\omega_z^{Ba}\right)^2\left(\epsilon^2 - \frac{1}{2} - \sum_{k=1,k\neq i}^{N}\frac{1}{|u_i - u_k|^3}\right), \quad m_{ion}^{(i,j)} = m_{Ba}, i = j, \tag{B6}$$

$$A'_{ij} = \frac{\left(\omega_z^{Ba}\right)^2}{\mu_m}\left(\frac{\epsilon^2}{\mu_m} - \frac{1}{2} - \sum_{k=1,k\neq i}^{N}\frac{1}{|u_i - u_k|^3}\right), \quad m_{ion}^{(i,j)} = m_{Yb}, i = j, \tag{B7}$$

$$A'_{ij} = \sqrt{\frac{1}{\mu_m}}\left(\omega_z^{Ba}\right)^2\left(\frac{1}{|u_i - u_j|^3}\right), \quad m_{ion}^i \neq m_{ion}^j. \tag{B8}$$

The motional modes $b_j^m$ and their corresponding mode frequencies $\omega_m$ should satisfy the following equation:

$$\sum_{i=1}^{N}A'_{ij}b_i^m = \omega_m^2 b_j^m, \tag{B9}$$

where $\omega_m$ is the transverse motional mode frequency and $b_j^m$ is the motional mode with $m = 1, \ldots, N$ being the motional mode index. Going back to the original set of coordinates $q_j$

for the $j$th ion, they have the following quantized form:

$$\hat{q}_j(t) = \frac{1}{\sqrt{m_{ion}^j}}\sum_{m=1}^{N}b_j^m\hat{Q}_m(t)$$

$$= i\sqrt{\frac{\hbar}{2m_{ion}^j\omega_m}}\sum_{m=1}^{N}b_j^m(\hat{a}_m e^{-i\omega_m t} - \hat{a}_m^\dagger e^{-i\omega_m t}). \tag{B10}$$

Note that the wavelength in the Lamb-Dicke parameter $\eta_j^m = b_j^m \Delta k_j \sqrt{\frac{\hbar}{2m_{\text{ion}}^j \omega_m}}$ is different for two species.

### 2. The infinite long uniform ion chain

As explained in the main text, our scheme is a linear iterative method, which can be easily applied to an infinite long uniform ion chain. Let us consider an infinite long ion chain along the $z$ axis with uniform spacing $d$, in the limit $N \to \infty$ and $\omega_z \to 0$, the periodic mixed-species exist discrete translational invariance under the transformation $j \mapsto j + P'$, where $P'$ is the size of the unit cell. Thus, we label the positions of ions as $(l, j)$ where unit-cell index $l \in \mathbb{Z}$ and position $j \in 1, ..., P'$ within a unit cell. In our calculations, within each

unit cell, the first two ions are $^{171}\text{Yb}^+$ ions and the remaining $P' - 2$ ions are $^{138}\text{Ba}^+$ ions.

To account for the translational invariance of the Hamiltonian in the unit-cell index $l$, we interpret the coordinates $\delta q_{l,j}$ as coefficients of a Fourier series, $c_{k,j} = \sum_{l \in \mathbb{Z}} e^{-ikl} \delta q_{l,j}$, where $k$ is analogous to the quasimomentum of an electron in a solid. In terms of the new complex coordinates $c_{k,j}$, the potential energy can be expressed

$$V = \int_{-\pi}^{\pi} \frac{dk}{2\pi} \sum_{j,j'=1}^{P'} \upsilon_{j,j'}^k c_{k,j}^* c_{k,j'}, \tag{B11}$$

with

$$\upsilon_{j,j'}^k = \left(\omega_x^{\text{Ba}}\right)^2 \left(1 - 2\zeta(3)\varsigma^2 - \sum_{l \in \mathbb{Z}, l \neq 0} \frac{\varsigma^2}{|pl|^3} e^{-ikl}\right), \quad m_{\text{ion}}^j = m_{\text{ion}}^{j'} = m_{\text{Ba}}, \tag{B12}$$

$$\upsilon_{j,j'}^k = \frac{\left(\omega_x^{\text{Ba}}\right)^2}{\mu_m} \left(\frac{1}{\mu_m} - 2\zeta(3)\varsigma^2 - \sum_{l \in \mathbb{Z}, l \neq 0} \frac{\varsigma^2}{|pl|^3} e^{-ikl}\right), \quad m_{\text{ion}}^j = m_{\text{ion}}^{j'} = m_{\text{Yb}}, \tag{B13}$$

$$\upsilon_{j,j'}^k = \sqrt{\frac{1}{\mu_m}} \left(\omega_x^{\text{Ba}}\right)^2 \left(\sum_{l \in \mathbb{Z}} \frac{\varsigma^2}{|pl + j - j'|^3} e^{-ikl}\right), \quad m_{\text{ion}}^j \neq m_{\text{ion}}^{j'}, \tag{B14}$$

where $\varsigma^2 = \frac{q^2}{4\pi \varepsilon_0 d^3 m_{\text{Ba}} (\omega_x^{\text{Ba}})^2}$, $q$ is the charge of an ion, and $\varepsilon_0$ is the permittivity of free space, $\zeta(3) = \sum_{j=1}^{j=\infty} \approx 1.202$ is the Riemann zeta function.

Next, we introduce new coordinates $b_{k,n} = \sum_{j=1}^{p} \mathbf{B}_j^{k,n*} c_{k,j}$, where $\mathbf{B}_j^{k,n}$ and their eigenvalues $\omega_{k,n}$ can be obtained by the diagonalization of $\upsilon_{j,j'}^k$. The motional modes can be represented as plane waves proportional to $e^{ikl}$ with quasimomentum $k$. Because they are complex and not independent, the quasimomentum can be restricted to the interval $k \in [0, \pi]$, which can guarantee that the motional mode vectors are real. We can decompose $b_{k,n}$ and $\mathbf{B}_j^{k,n}$ into real and imaginary parts, $b_{k,n} = 1/\sqrt{2}(\xi_{k,n,1} + i\xi_{k,n,2})$ and $\mathbf{B}_j^{k,n} = \Xi_j^{k,n,1} + i\Xi_j^{k,n,2}$, to obtain

$$\delta q_{l,j} = \int_0^{\pi} \frac{dk}{2\pi} \sum_{n=1}^{p} \sum_{\lambda=1}^{2} \mathbf{\Pi}_{l,j}^{k,n,\lambda} \xi_{k,n,\lambda}. \tag{B15}$$

$\xi_{k,n,\lambda}$ are the desired real and independent mode coordinates, and the motional mode transformation matrices are given by

$$\mathbf{\Pi}_{l,j}^{k,n,1} = \sqrt{2}\left[\cos(kl)\Xi_j^{k,n,1} - \sin kl \, \Xi_j^{k,n,2}\right], \tag{B16}$$

$$\mathbf{\Pi}_{l,j}^{k,n,2} = -\sqrt{2}\left[\cos(kl)\Xi_j^{k,n,2} - \sin kl \, \Xi_j^{k,n,1}\right]. \tag{B17}$$

The motional modes and the corresponding mode frequencies for an infinite long uniform ion chain is illustrated in terms of the mode matrix $\mathbf{\Pi}_{l,j}^{k,n,\lambda}$ in Figs. 6(a) and 6(b) for $l = 1, k = \frac{\pi}{3}, \lambda = 1, 2$. The localization is similar to that of the finite periodic mixed-species ion chain, shown in the main text. Additionally, the calculation of motional modes in infinite long uniform mixed-species chain is similar to the

tweezer arrays [39]. The modes of the two species are almost independent which means that, modes of $n = 5$ and $n = 6$, which correspond, respectively, to COM and stretch motions of the computational ions is separated with the other modes, which involve the ancillary ions within a unit cell. In particular, the localized COM and stretch modes of the computational ion pairs in different unit cells hybridize uniformly. The bands of mode frequency split up into $p = 6$ bands due to the mass ratio where the lowest two bands correspond to COM and stretch modes of computational ion pairs. In our calculations, we define the mean frequencies of COM band as $\omega_1$ and the mean frequencies of stretch band as $\omega_2$.

### APPENDIX C: THE APPLICATIONS OF THE MIXED-SPECIES ION CHAIN

In this Appendix, we list some important applications of the mixed-species ion chain in our scheme. The main thing is
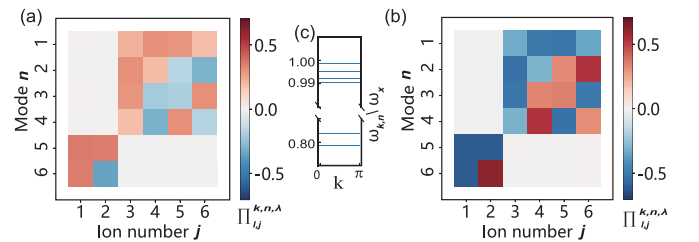


FIG. 6. (a) The transverse motional modes of a uniform mixed-species ion chain with $P' = 6$ within a unit cell where $l = 1, k = \frac{\pi}{3}$, and $\lambda = 1$. (b) The transverse motional modes for $l = 1, k = \frac{\pi}{3}$, and $\lambda = 2$. (c) The corresponding mode frequency spectrum $\omega_{k,n}/\omega_x$ is shown in middle inset.
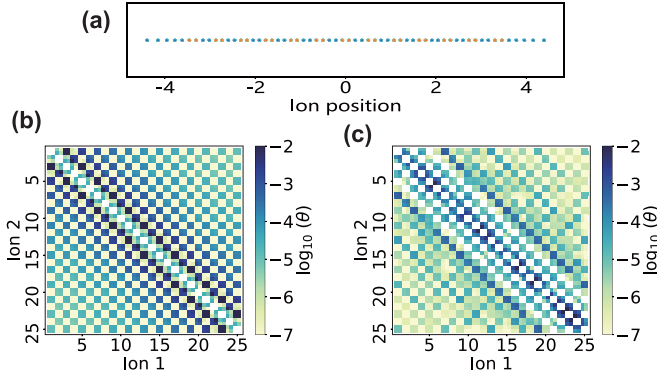
FIG. 7. (a) The periodic $^{171}$Yb$^+$/$^{138}$Ba$^+$ mixed-species ion chain where $^{171}$Yb$^+$ act as computational and $^{138}$Ba$^+$ as ancillary qubits. (b) The crosstalk within each pair of ions of the $G = 1$ with the corresponding pulse segments $N_{\text{seg}} = 7$ with $\mu_{\text{Yb}} = 0.8\omega_x$, $\mu_{\text{Ba}} = 0.984\omega_x$, $\tau_{\text{Yb}} = 100$ μs, $\tau_{\text{Ba}} = 100$ μs. (c) The crosstalk within each pair of ions of the $G = 3$ with the corresponding pulse segments $N_{\text{seg}} = 20$.

the motional mode structure. We utilize the localized motional modes and the gapped mode frequencies of the mixed-species ion chain to greatly reduce the number of constraints of the quantum gates and lower the crosstalk between the different species ions, such as $^{171}$Yb$^+$ and $^{138}$Ba$^+$.

In our scheme, another advantage is that the $^{138}$Ba$^+$ ions can also be applied the corresponding lasers to perform two-qubit gates. In other words, we can perform independently optimized gates simultaneously on both sets of ions to realize a maximally dense quantum circuit. Crosstalk between these two species of ions is naturally suppressed due to the small spatial overlap of the respective modes. For example, we consider a chain of 60 ions with five buffer ions at each edge and choose the ion period distance $P = 2$ to implement 25 entangling pairs in total, which contains 13 entangling $^{171}$Yb$^+$ pairs and 12 entangling $^{138}$Ba$^+$ pairs. We present the crosstalk within each pair of computational ions of the $G = 1$ with the corresponding pulse segments $N_{\text{seg}} = 7$ and $G = 3$ with $N_{\text{seg}} = 20$, $\mu_{\text{Yb}} = 0.8\omega_x$, $\mu_{\text{Ba}} = 0.984\omega_x$, $\tau_{\text{Yb}} = 100$ μs, $\tau_{\text{Ba}} = 100$ μs. As we can see in Fig. 7, the crosstalk between these two species of ions is naturally suppressed when independently optimized gates simultaneously on both sets of ions.

In addition, cotrapping ancillary ions for sympathetically cooling the computational ions can effectively suppress the axial motional heating effect, which is even more severe for a long chain due to the weak axial confinement. The long ion chain requires highly anisotropic trapping potentials which are typically achieved by lowering the axial confinement, resulting in high motional occupation numbers after the Doppler cooling and a high heating rate of the center-of-mass (COM) axial motion. The fidelity of quantum gate operations can then be limited by the weak axial confinement and the heating effects. Since the direct cooling will destroy the qubit state, and this problem will be more serious when the ion chain is longer. The sympathetic cooling in mixed-species trapped ion systems can solve this problem efficiently which has been discussed in Ref. [38]. The axial heating of the ion chain can be suppressed by interspersing the operations with periodic sympathetic cooling of axial modes via ancillary ions that

are distributed throughout the ion chain through the Coulomb interaction. Cooling one species of ion will not disturb the other ion's state due to the fact that the cooling lasers for different species of ions are different.

## APPENDIX D: POWER-OPTIMAL METHOD

By using the ANS, the spin-motion decoupling constraints are roughly satisfied which means that we can achieve infidelity of the two-qubit gate below the infidelity threshold $\delta F_t$. Additionally, the approximated null subspace guarantees that the crosstalk within the neighboring pairs is eliminated to 0. Therefore, we wish to minimize the laser power, in other words, the RMS Rabi frequency, by carefully considering the experimental feasibility in realizing the effective Rabi frequency.

The power-optimal method [40] in our approach is based on finding the smallest sum of squares of $\mathbf{\Omega}$ under the accumulated phase constraint for every computational ion pair using the $V$ degrees of freedom of the approximated null subspace $\mathbf{\Omega}_{\text{anss}}^{[j,j']}$, where $[j, j'] \in J$ is the label of the entangled pairs. Our goal now is to linearly combine the orthonormal solution space vectors with real expansion amplitudes $\mathbf{\Gamma}$ to find the power-optimal solution,

$$\mathbf{\Omega}_{\text{opt}}^{[j,j']} = \sum_{\nu=1}^{V} \Gamma_\nu (\mathbf{\Omega}_{\text{s}})_\nu, \qquad (\text{D1})$$

where $\mathbf{\Omega}_{\text{s}}$ represents the subspace of ANS $\mathbf{\Omega}_{\text{anss}}^{[j,j']}$.

The root-mean-square (RMS) Rabi frequency power $P_r$ can be expressed as

$$P_r^2 = \frac{1}{N_{\text{seg}}} \sum_{n=1}^{N_{\text{seg}}} \Omega_n^2 = \frac{1}{N_{\text{seg}}} \mathbf{\Omega}^T \mathbf{I} \mathbf{\Omega}, \qquad (\text{D2})$$

where $\mathbf{I}$ is the $N_{\text{seg}} \times N_{\text{seg}}$ identity matrix.

Now, we can formulate the constrained optimization problem as

$$f(\Gamma) = \min((\mathbf{\Gamma}^{[j,j']})^T \mathbf{H} \mathbf{\Gamma}^{[j,j']})$$

$$\text{s.t.} |(\mathbf{\Gamma}^{[j,j']})^T \mathbf{R}^{[j,j']} \mathbf{\Gamma}^{[j,j']}| = \frac{\pi}{4}, \qquad (\text{D3})$$

where

$$\mathbf{H} = \mathbf{\Omega}_{\text{s}}^T \mathbf{I} \mathbf{\Omega}_{\text{s}}, \qquad (\text{D4})$$

$$\mathbf{R}^{[j,j']} = \mathbf{\Omega}_{\text{s}}^T \mathbf{D}^{[j,j']} \mathbf{\Omega}_{\text{s}}. \qquad (\text{D5})$$

Geometrically, the coupling strength constraint in Eq. (D3) is a $V$-dimensional hypersurface and the minimum of laser power in Eq. (D3) is a $V$-dimensional hypersphere. The minimum objective function is that the hypersphere is inscribed in the hypersurface and just touches the hypersurface along the principal axis with the smallest length. In other words, the eigenvector corresponding to the largest eigenvalue $v_{\text{max}}$ will be the optimal solution $\mathbf{\Gamma}$. In this way, our optimization problem is solved:

$$\mathbf{\Omega}_{\text{opt}}^{[j,j']} = \mathbf{\Omega}_{\text{opt}}^j = \mathbf{\Omega}_{\text{opt}}^{j'} = \left| \frac{\pi}{4 v_{\text{max}}} \right|^{\frac{1}{2}} \sum_{\nu=1}^{V} \Gamma_\nu (\mathbf{\Omega}_{\text{s}})_\nu. \qquad (\text{D6})$$

## APPENDIX E: ROBUSTNESS CONSTRAINTS

In addition to ensuring that all excited modes are roughly decoupled, i.e., a high fidelity under ideal operating conditions, it is also critical to ensure the entangling gate operation is robust against various types of external parameters errors. Here we give a detailed introduction of the robustness constraint against random drifts of motional frequencies, considered in the main text. In experiments, the motional mode frequencies $\omega_m$ can drift due to some uncontrollable effects, such as stray electromagnetic fields. Thus, one requires that

$$\frac{\partial^k \alpha_j^m}{\partial \omega_m^k} = 0, \quad m = 1, \ldots, N, \tag{E1}$$

or, in matrix notation,

$$\mathbf{Q}_m^{(k)} \mathbf{\Omega} = \mathbf{0}, \tag{E2}$$

where $\mathbf{Q}_m^{(k)}$ is the $2N \times N_{\text{seg}}$ coefficient matrix including the stabilization of the $m$th motional mode and the $j$th ion against drifts to an arbitrary stabilization order $k = 1, \ldots, K_\omega$.

Since the robust constraints which are related to the spin-motion residual coupling are linear in the Rabi frequency $\mathbf{\Omega}$, we can expand the matrix $\mathbf{M}$ to include these constraints

under the consideration of robustness in the calculation of the ANS, at the cost of additional degrees of freedom. More importantly, since the calculation of every motional mode is independent, one can achieve stabilization against random static fluctuations (i.e., individual mode drifts) independently with different signs of direction.

In the case of the random static drifts, which is more close to the experimental drifts, we choose $N$ random numbers $N_{\text{random}}$ from a Gaussian distribution with zero mean and standard deviation 1. Thus, all mode frequencies drift randomly according to $\boldsymbol{\omega}$ to $\boldsymbol{\omega} + \delta\omega_c N_{\text{random}}$, where $\delta\omega_c$ is a scaling factor and $\boldsymbol{\omega}$ is all motional mode frequencies. For a fair comparison, we repeat the random process six times and then average the infidelity.

Similarly, to stabilize against gate duration errors and laser detuning errors, one requires

$$\frac{\partial^l \alpha_j^m}{\partial \tau^l} = \frac{\partial^p \alpha_j^m}{\partial \mu^p} = 0, \quad m = 1, \ldots, N. \tag{E3}$$

Finally, one can also improve the robustness against the mixed drifts by including the corresponding constraints simultaneously.

[1] T. Monz, D. Nigg, E. A. Martinez, M. F. Brandl, P. Schindler, R. Rines, S. X. Wang, I. L. Chuang, and R. Blatt, Science **351**, 1068 (2016).

[2] A. Steane, Fortschr. Phys. **46**, 443 (1998).

[3] L. Postler, S. Heußen, I. Pogorelov, M. Rispler, T. Feldker, M. Meth, C. D. Marciniak, R. Stricker, M. Ringbauer, R. Blatt et al., Nature (London) **605**, 675 (2022).

[4] C. Figgatt, A. Ostrander, N. M. Linke, K. A. Landsman, D. Zhu, D. Maslov, and C. Monroe, Nature (London) **572**, 368 (2019).

[5] N. Grzesiak, R. Blümel, K. Wright, K. M. Beck, N. C. Pisenti, M. Li, V. Chaplin, J. M. Amini, S. Debnath, J.-S. Chen, and Y. Nam, Nat. Commun. **11**, 2963 (2020).

[6] P. Zhao, K. Linghu, Z. Li, P. Xu, R. Wang, G. Xue, Y. Jin, and H. Yu, PRX Quantum **3**, 020301 (2022).

[7] D. Bluvstein, H. Levine, G. Semeghini, T. T. Wang, S. Ebadi, M. Kalinowski, A. Keesling, N. Maskara, H. Pichler, M. Greiner et al., Nature (London) **604**, 451 (2022).

[8] S. J. Evered, D. Bluvstein, M. Kalinowski, S. Ebadi, T. Manovitz, H. Zhou, S. H. Li, A. A. Geim, T. T. Wang, N. Maskara et al., arXiv:2304.05420.

[9] J. I. Cirac and P. Zoller, Phys. Rev. Lett. **74**, 4091 (1995).

[10] C. D. Bruzewicz, J. Chiaverini, R. McConnell, and J. M. Sage, Appl. Phys. Rev. **6**, 021314 (2019).

[11] P. Wang, C.-Y. Luan, M. Qiao, M. Um, J. Zhang, Y. Wang, X. Yuan, M. Gu, J. Zhang, and K. Kim, Nat. Commun. **12**, 6948 (2021).

[12] T. P. Harty, D. T. C. Allcock, C. J. Ballance, L. Guidoni, H. A. Janacek, N. M. Linke, D. N. Stacey, and D. M. Lucas, Phys. Rev. Lett. **113**, 220501 (2014).

[13] C. J. Ballance, T. P. Harty, N. M. Linke, M. A. Sepiol, and D. M. Lucas, Phys. Rev. Lett. **117**, 060504 (2016).

[14] J. P. Gaebler, T. R. Tan, Y. Lin, Y. Wan, R. Bowler, A. C. Keith, S. Glancy, K. Coakley, E. Knill, D. Leibfried, and D. J. Wineland, Phys. Rev. Lett. **117**, 060505 (2016).

[15] C. R. Clark, H. N. Tinkey, B. C. Sawyer, A. M. Meier, K. A. Burkhardt, C. M. Seck, C. M. Shappert, N. D. Guise, C. E. Volin, S. D. Fallek et al., Phys. Rev. Lett. **127**, 130505 (2021).

[16] Y. Lu, S. Zhang, K. Zhang, W. Chen, Y. Shen, J. Zhang, J.-N. Zhang, and K. Kim, Nature (London) **572**, 363 (2019).

[17] C. D. Bentley, H. Ball, M. J. Biercuk, A. R. Carvalho, M. R. Hush, and H. J. Slatyer, Adv. Quantum Technol. **3**, 2000044 (2020).

[18] A. Sørensen and K. Mølmer, Phys. Rev. Lett. **82**, 1971 (1999).

[19] S.-L. Zhu, C. Monroe, and L.-M. Duan, Europhys. Lett. **73**, 485 (2006).

[20] G.-D. Lin, S.-L. Zhu, R. Islam, K. Kim, M.-S. Chang, S. Korenblit, C. Monroe, and L.-M. Duan, Europhys. Lett. **86**, 60004 (2009).

[21] S.-L. Zhu, C. Monroe, and L.-M. Duan, Phys. Rev. Lett. **97**, 050505 (2006).

[22] Y. Wu, S.-T. Wang, and L.-M. Duan, Phys. Rev. A **97**, 062325 (2018).

[23] A. R. Milne, C. L. Edmunds, C. Hempel, F. Roy, S. Mavadia, and M. J. Biercuk, Phys. Rev. Appl. **13**, 024022 (2020).

[24] T. J. Green and M. J. Biercuk, Phys. Rev. Lett. **114**, 120502 (2015).

[25] S.-C. Liu, L. Cheng, G.-Z. Yao, Y.-X. Wang, and L.-Y. Peng, Phys. Rev. E **107**, 035304 (2023).

[26] P. H. Leung, K. A. Landsman, C. Figgatt, N. M. Linke, C. Monroe, and K. R. Brown, Phys. Rev. Lett. **120**, 020501 (2018).

[27] Y. Wang, S. Crain, C. Fang, B. Zhang, S. Huang, Q. Liang, P. H. Leung, K. R. Brown, and J. Kim, Phys. Rev. Lett. **125**, 150505 (2020).

[28] M. Kang, Q. Liang, B. Zhang, S. Huang, Y. Wang, C. Fang, J. Kim, and K. R. Brown, Phys. Rev. Appl. **16**, 024039 (2021).

[29] P. H. Leung and K. R. Brown, Phys. Rev. A **98**, 032318 (2018).

[30] K. A. Landsman, Y. Wu, P. H. Leung, D. Zhu, N. M. Linke, K. R. Brown, L. Duan, and C. Monroe, Phys. Rev. A **100**, 022332 (2019).

[31] R. Blümel, N. Grzesiak, N. Pisenti, K. Wright, and Y. Nam, npj Quantum Inf. **7**, 147 (2021).

[32] J. P. Home, Adv. At. Mol. Opt. Phys. **62**, 231 (2013).

[33] D. Kielpinski, B. E. King, C. J. Myatt, C. A. Sackett, Q. A. Turchette, W. M. Itano, C. Monroe, D. J. Wineland, and W. H. Zurek, Phys. Rev. A **61**, 032310 (2000).

[34] G.-D. Lin and L.-M. Duan, Quantum Inf. Process. **15**, 5299 (2016).

[35] I. V. Inlek, C. Crocker, M. Lichtman, K. Sosnova, and C. Monroe, Phys. Rev. Lett. **118**, 250502 (2017).

[36] D. B. Hume, T. Rosenband, and D. J. Wineland, Phys. Rev. Lett. **99**, 120502 (2007).

[37] Z.-C. Mao, Y.-Z. Xu, Q.-X. Mei, W.-D. Zhao, Y. Jiang, Y. Wang, X.-Y. Chang, L. He, L. Yao, Z.-C. Zhou *et al.*, Phys. Rev. Lett. **127**, 143201 (2021).

[38] M. Cetina, L. N. Egan, C. Noel, M. L. Goldman, D. Biswas, A. R. Risinger, D. Zhu, and C. Monroe, PRX Quantum **3**, 010334 (2022).

[39] T. Olsacher, L. Postler, P. Schindler, T. Monz, P. Zoller, and L. M. Sieberer, PRX Quantum **1**, 020316 (2020).

[40] L. Cheng, S.-C. Liu, L. Geng, Y.-K. Fang, and L.-Y. Peng, Phys. Rev. A **107**, 042617 (2023).

[41] T. Choi, S. Debnath, T. A. Manning, C. Figgatt, Z.-X. Gong, L.-M. Duan, and C. Monroe, Phys. Rev. Lett. **112**, 190502 (2014).